Statistical Evaluation of Satellite Ocean Color Data Retrievals

Karlis Mikelsons,[1,2,*] Menghua Wang,[1] and Lide Jiang[1,3]

[1]NOAA National Environmental Satellite, Data, and Information Service
Center for Satellite Applications and Research
E/RA3, 5830 University Research Court
College Park, MD 20740, USA

[2]Global Science and Technology, Inc., Greenbelt, Maryland 20770, USA

[3]CIRA, Colorado State University, Fort Collins, CO 80523, USA

*Corresponding author: Karlis.Mikelsons@noaa.gov

Remote Sensing of Environment

Revised on 11/26/2019

ABSTRACT

We develop a statistical approach to evaluate the performance of the ocean color data processing system for satellite-derived ocean color data products based on temporal stability of retrievals. We use the Multi-Sensor Level-1 to Level-2 (MSL12) ocean color data processing system to obtain the normalized water-leaving reflectance $\rho_{wN}(\lambda)$ spectra from the Visible Infrared Imaging Radiometer Suite (VIIRS) measurements. The deviations of $\rho_{wN}(\lambda)$ spectra from temporally and spatially averaged values are investigated, and the statistics with respect to various retrieval parameters are collected, including the solar-sensor geometry (solar-zenith, sensor-zenith, and relative azimuth angles), and various ancillary data (surface wind speed, surface atmospheric pressure, water vapor amount, and ozone concentration). The performance of MSL12 is also evaluated with respect to other intermediate retrieval parameters. The study shows that MSL12 produces statistically consistent VIIRS ocean color retrievals in the global open ocean, with respect to retrieval geometry parameters, as well as the ancillary inputs.

Keywords: Ocean color remote sensing, atmospheric correction, data processing, and VIIRS.

1. Introduction

Ocean color remote sensing from space is a rapidly growing field with several new polar orbiting instruments launched and recently deployed for routine global ocean property measurements and monitoring, including the Visible Infrared Imaging Radiometer Suite (VIIRS) on the Suomi National Polar-orbiting Partnership (SNPP) and NOAA-20 satellites, the Ocean and Land Colour Instrument (OLCI) on the Sentinel-3A and Sentinel-3B satellites, and the Second-Generation Global Imager (SGLI) on the Global Change Observation Mission-Climate (GCOM-C) satellite. In particular, VIIRS-SNPP, launched on October 28, 2011, is the first VIIRS in the series that are all planned to provide decades long consistent global atmosphere, land, cryosphere, and ocean Environmental Data Records (EDR or Level-2 data) (*Goldberg et al.*, 2013). To ensure accurate routine production of global ocean optical, biological, and biogeochemical properties, a considerable effort has been made towards sensor on-orbit instrument calibration (*Cao et al.*, 2013; *Sun and Wang*, 2015; 2016), on-orbit vicarious calibration using the in situ optics data from the Marine Optical Buoy (MOBY) in the waters off Hawaii (*Clark et al.*, 1997; *Wang et al.*, 2016), development and improvement of ocean color retrieval algorithms (*Jiang and Wang*, 2014; *Wang and Jiang*, 2018; *Wang et al.*, 2012; *Wang and Son*, 2016), and VIIRS ocean color product data evaluation and validation (*Barnes et al.*, 2019; *Hlaing et al.*, 2013; *Wang et al.*, 2013).

Deriving global ocean optical, biological, and biogeochemical property data from space-based measurements is a very complicated and challenging task, which requires close attention to instrument calibration (including vicarious calibration), algorithm development, and the validation of the results (*McClain*, 2009). The spaceborne radiometers directly measure the top of the atmosphere (TOA) radiances, which in addition to the water color signal also include radiance contributions from various light scattering processes in the atmosphere, and reflection and refraction from the water surface. Extracting the ocean color spectra from the TOA radiance spectra is known as atmospheric correction (*Gordon and Wang*, 1994a; *IOCCG*, 2010; *Wang*, 2007), and it involves subtraction of these different radiance contributions, which are much larger than the ocean color signal (*Gordon and Wang*, 1994a; *IOCCG*, 2010; *Wang*, 2007).

Furthermore, these terms depend on multiple parameters, such as solar-sensor geometry, but also physical or meteorological conditions, such as surface wind speed, atmospheric pressure, atmospheric ozone concentration, and column water vapor amount (*Ramachandran and Wang*, 2011). Due to the overall complexity and the multiple parameters involved in the atmospheric correction process, comparisons with in situ ocean color measurements are integral and important to maintain good quality of the ocean color satellite data retrievals (*Werdell and Bailey*, 2005).

In situ measurements, however, also have significant limitations. First, the number of in situ measurements is several orders of magnitude less than the number of satellite remote sensing retrievals. Second, in situ measurements are usually confined to a few stations in the regions of interest, while cruises with more variety of sampling stations are not as frequent. This means that most geographical ocean regions and times are never represented in the available in situ data. Furthermore, in situ data also involve measurement uncertainties (*Werdell and Bailey*, 2005; *Zibordi et al.*, 2009; *Zibordi et al.*, 2015), sometimes even with large uncertainties in data quality.

One possibility to address these limitations is to perform an inter-sensor comparison (*Barnes and Hu*, 2016; *Wang et al.*, 2002; *Zibordi et al.*, 2006). However, it is not easy to attribute the discrepancies to a particular sensor, especially since the older and more thoroughly studied sensors often have also suffered more degradation due to longer time in service. In addition, differences in sensor calibration may be difficult if not impossible to disentangle from the differences in performance of the retrieval algorithms.

The main idea of this work is to use ocean color data from the same sensor over large swaths of the global open ocean, where water conditions are relatively uniform, and temporal changes are more gradual, to evaluate the statistical consistency of the ocean color retrievals. Yet, even within the relatively uniform conditions of the open ocean, ocean optical, biological, and biogeochemical properties can have a large spatial variation over longer length scales, as well as a significant seasonal variation. Therefore, it is the deviation from the spatial and temporal average, or anomaly, that can provide the information about the biases and consistency of ocean color data retrievals for the particular space-time domain. It is assumed that, for perfect retrievals, little to no deviations from such an average are expected.

The relevant spatial and temporal length scales of the average need to be long enough to provide enough data for a meaningful and consistent average (given that often retrievals are not possible or are masked out due to clouds (*King et al.*, 2013), high sun glint contamination (*Wang and Bailey*, 2001), straylight effect (*Jiang and Wang*, 2013), high solar- and sensor-zenith angles (*Mikelsons and Wang*, 2019), or other conditions. The length scale must be smaller than the relevant scale of physical phenomena in water (such as ocean currents, mesoscale eddies, algal blooms, etc.). The time scale for calculating the average also needs to be shorter than the corresponding time scales of physical processes. At the very least, it should be able to resolve the seasonal variation, which is the most important temporal cycle resolvable by daily satellite observations.

In this study, it is assumed that the ocean physical processes with comparatively short-time scales, such as diurnal changes, are relatively small in the open ocean over the hourly time scale. The orbital period of polar orbiting Earth observing satellites is about 100 minutes, and the variation of the local time of satellite overpass from day to day is roughly of the same time scale. Thus, we assume that the diurnal changes are comparatively small within this time scale. Indeed, matchups with in situ data measured within hours of satellite overpass are often used to check data quality (*Wang et al.*, 2009b; *Werdell and Bailey*, 2005).

It should be pointed out that this method has limitations — it can only measure satellite data statistical consistency. It cannot, for example, detect any long-term trends in ocean color measurements, nor any changes or irregularities of the radiance spectral shape (*Wei et al.*, 2016).

2. Methodology

2.1. The MSL12 ocean color data processing system

The Multi-Sensor Level-1 to Level-2 (MSL12) is the current routine ocean color data product retrieval system used at NOAA. In particular, VIIRS-SNPP and VIIRS-NOAA-20 global ocean color products have been routinely produced using the MSL12 ocean color data processing system since their successful launches in October 2011 and November 2017, respectively. MSL12 is an enterprise ocean color data processing system, and the software is based on the NASA Sea-viewing Wide Field-of-view Sensor (SeaWiFS) Data Analysis System (SeaDAS) version 4.6 with several updates and modifications. MSL12 is designed to provide consistent ocean color retrievals by employing the same retrieval algorithms for multiple satellite sensors (*Wang, et al.*, 2002). Specifically, in this study, we use the near-infrared (NIR)-based atmospheric correction in MSL12 (*Gordon and Wang*, 1994a; *Wang, et al.*, 2013) with the improved NIR ocean reflectance correction algorithm (*Jiang and Wang*, 2014), which combines the three other NIR water reflectance correction algorithms (*Bailey et al.*, 2010; *Ruddick et al.*, 2000; *Wang, et al.*, 2012). However, it should be noted that for global open ocean waters the NIR ocean reflectance contribution is generally negligible, thus the NIR reflectance correction in the ocean color data processing is not important.

The main VIIRS ocean color data products derived by MSL12 are the normalized water-leaving radiance spectra, $nL_w(\lambda)$, which are equivalent to the water-leaving radiances measured on the ocean surface assuming no atmosphere and the Sun at the zenith (*Gordon*, 2005; *Morel and Gentili*, 1996; *Wang*, 2006). The $nL_w(\lambda)$ spectra are subject to destriping to remove striping artifacts (*Mikelsons et al.*, 2014). The destriped $nL_w(\lambda)$ spectra are then used to further derive ocean biological and biochemical property data, such as chlorophyll-a (Chl-a) concentration (*Hu et al.*, 2012; *O'Reilly et al.*, 1998; *Wang and Son*, 2016), water diffuse attenuation coefficient at the wavelength of 490 nm $K_d(490)$ (*Lee et al.*, 2005; *Wang et al.*, 2009a), and for the domain of the photosynthetically available radiation (PAR) $K_d(\mathrm{PAR})$ (*Son and Wang*, 2015). Other data products, such as aerosol optical depth (AOD) (*Wang et al.*, 2005) and the aerosol Angstrom coefficient (*Angstrom*, 1929), characterize aerosol properties, and are also used in atmospheric correction (*IOCCG*, 2010; *Wang, et al.*, 2005). In this study, we convert the $nL_w(\lambda)$ spectra to the normalized water-leaving reflectance spectra, defined as $\rho_{wN}(\lambda) = \pi\, nL_w(\lambda)/F_0(\lambda)$, where $F_0(\lambda)$ is the extraterrestrial solar irradiance (*Thuillier et al.*, 2003). This way, the ocean color spectra can be more equally compared spectrally (*Gordon and Wang*, 1994a).

On input, MSL12 requires the TOA radiances measured by the sensor, i.e., VIIRS Sensor Data Records (SDR, or Level-1B data), as well as ancillary data characterizing the atmospheric and ocean surface conditions to aid the retrievals (*Ramachandran and Wang*, 2011). The sensor-measured TOA radiances need to be properly calibrated (*Cao, et al.*, 2013; *Sun and Wang*, 2015; 2016). In addition, complete geolocation information is required (latitude and longitude for each retrieval sample), as well as information about retrieval geometry, which includes the solar- and sensor-zenith angles, as well as the relative azimuth angle.

The main ancillary data are the sea level atmospheric pressure, surface wind speed, the amount of ozone and water vapor in the atmosphere, integrated over the altitude (*Ramachandran and Wang*, 2011). Using more accurate ancillary data, such as those produced by the NOAA Global Forecasting System (GFS) has been shown to increase the accuracy of the ocean color products (*Ramachandran and Wang*, 2011).

2.2. Evaluation approach and criteria

The VIIRS-SNPP SDR (or Level-1B data) from the year 2016 were processed to produce global ocean color product data using the MSL12 ocean color data processing system. We work with $\rho_{wN}(\lambda)$ spectra, but the entire procedure can also be applied to the normalized water-leaving radiance $nL_w(\lambda)$ spectra (or remote sensing reflectance $R_{rs}(\lambda)$ spectra, defined as $R_{rs}(\lambda) = nL_w(\lambda)/F_0(\lambda)$), since these only differ by constant conversion factors. Data obtained with other retrieval algorithms, or even from different sensors can also be analyzed using this method.

The first step is to establish a baseline for temporal and spatial averaged $\rho_{wN}(\lambda)$ data. For each day of retrievals, the global Level-2 $\rho_{wN}(\lambda)$ data are binned into a global Level-3 daily average (*Campbell et al.*, 1995). We use a particular kind of grid that covers the entire globe with bins of nearly equal area. Within this grid, the bins are arranged into rows, such that an integer number of rows fit within the 180º of latitude. For example, the 9 km bins used in this study cover 5 minutes in latitude. Thus, 2160 rows of the 9 km bins span the entire 180º of latitude. The longitudinal size of bins is determined as the closest match to the extent in the latitude (thus ensuring nearly square shaped bins) that also fits an integer number of bins within the row spanning the entire 360º of longitude, for each row of bins. Thus, with 9 km bins, there are 4320 bins per one row on the equator. This number decreases towards the poles as a cosine function of the latitude.

In the binning process, we use several masks and data quality flags, e.g., land, cloud (*Wang and Shi*, 2006), straylight (*Jiang and Wang*, 2013), high sun glint contamination (*Wang and Bailey*, 2001), etc., to discard poor quality retrievals due to various conditions in order to obtain the most accurate binned data product for all ocean color data, e.g., $\rho_{wN}(\lambda)$ [or $nL_w(\lambda)$], Chl-a, $K_d(490)$, etc.

In the following step, a weighted temporal moving average is calculated for each bin using the daily binned data for the time average period T_a = 17 days from 8 days before and 8 days after the particular day. We weight the time average with a cosine function of time difference Δt, measured in days, i.e., $w(\Delta t) = \cos[\pi \Delta t/(T_a + 1)]$. This choice of weighting function emphasizes the importance of the data closer to a given time, however, other weighting functions can also be used, with qualitatively similar results. The choice of time period T_a is motivated by the SNPP revisit cycle of 16 days.

Once the spatially binned and time averaged baseline data are obtained, the anomaly can be calculated. But, before that, we filter the $\rho_{wN}(\lambda)$ data to discard the coastal areas from the statistical analysis due to their much shorter temporal and spatial scales of variability. To have a simple criterion, we choose to only use the ocean color retrievals from locations with water depth exceeding 1 km (i.e., global deep-water regions). Furthermore, we again exclude data with high sun glint conditions, and other conditions severely affecting the retrieval quality. However, we include data with high solar- and sensor-zenith angles to estimate the effect of such conditions on the derived ocean color products.

For each of the filtered retrieval data points, the corresponding spatial-temporal average calculated in the previous step is subtracted, yielding the anomaly $\Delta\rho_{wN}(\lambda, s, t)$ (s and t denote space and time dependence, respectively). We also look up the corresponding values of various geometrical, ancillary, and physical parameters $p_i(s,t)$ for each retrieval. The anomaly, $\Delta\rho_{wN}(\lambda, s, t)$ is then recorded in histograms to analyze its dependence on parameters p_i. For each histogram, we calculate the mean anomaly $\Delta\rho_{wN}(\lambda, p_i)$ over all retrievals that fall in the same bin of the parameter p_i. The total number of data points in each histogram bin of the dependent parameter p_i is also recorded. The major steps of this statistical analysis are schematically depicted in Fig. 1.

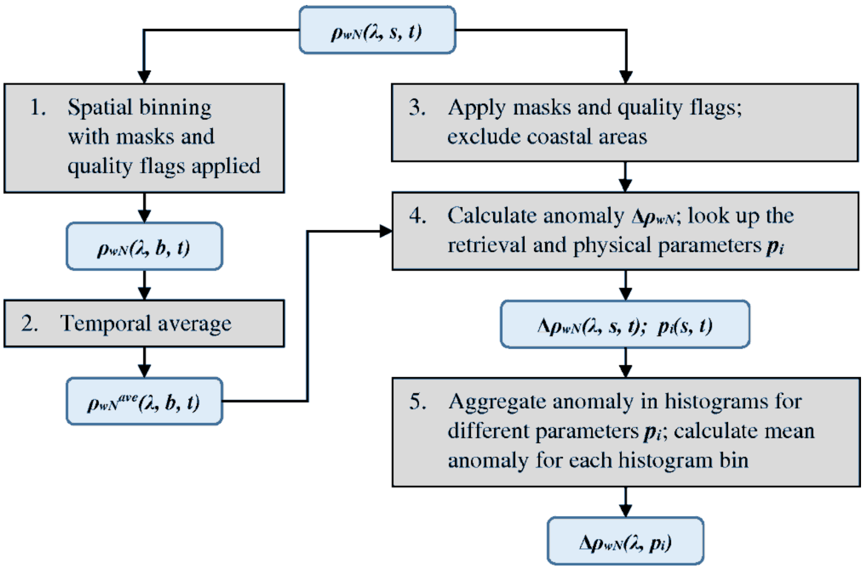

Figure 1. Diagram summarizing the steps of the statistical analysis. Indices s and t denote space and time dependence of the Level-2 data, respectively. The index b denotes spatial bin. The parameters p_i denote all retrieval and physical parameters included in this study. The quality flags in the step 3 may differ from those in the step 1.

For good quality ocean color retrievals, the mean anomaly $\Delta\rho_{wN}(\lambda, p_i)$ [further denoted as $\Delta\rho_{wN}(\lambda)$] is expected to be close to zero across the entire range of any dependent parameter p_i. A significant departure from zero in anomaly (compared to the retrieval accuracy requirements) indicates either an underestimate or an overestimate of $\rho_{wN}(\lambda)$ spectra under certain conditions characterized by the corresponding dependent variable p_i. We note that the accuracy requirement of satellite-derived $\rho_{wN}(\lambda)$ spectra for the global open ocean is that $\Delta\rho_{wN}(\lambda)$ in the blue (443 nm band) < ~0.001 (or 5%) (*Gordon and Wang*, 1994a; *IOCCG*, 2010; *Wang*, 2007). In addition to the mean anomaly, we also collect statistics and monitor the variance of the anomaly. Lower variance usually implies more precise retrievals for a given parameter range.

We note that results for the reflectance anomaly $\Delta\rho_{wN}(\lambda)$ are not sensitive to the exact choice of T_a, or the type of time averaging used, nor to the spatial bin size. However, the variance of the $\Delta\rho_{wN}(\lambda)$ increases with averaging over longer time period (T_a=33), and larger spatial bin size (18km), because natural fluctuations and changes of $\rho_{wN}(\lambda)$ over longer temporal and spatial scales are included into the average.

3. Results

The relevant parameters to ocean color retrievals can roughly be divided into three groups: the parameters describing the solar-sensor geometry with respect to the observable water surface, the ancillary parameters, and the intermediate parameters describing the retrieval conditions.

3.1. Solar-sensor geometry effect

We first evaluate the consistency of retrievals with respect to the solar-sensor geometry angles. Figure 2a shows the dependence of $\Delta\rho_{wN}(\lambda)$ on the sensor-zenith angle. Unsurprisingly, $\Delta\rho_{wN}(\lambda)$ is smaller for lower values of this angle, but it becomes significantly negative for sensor-zenith angles over 60^o, which means that $\rho_{wN}(\lambda)$ spectra are underestimated for these conditions. From results in Fig. 2a, it appears that the currently used threshold value for sensor-zenith angle of 60^o in MSL12 is a reasonable choice to separate good retrievals from poor or questionable ones.

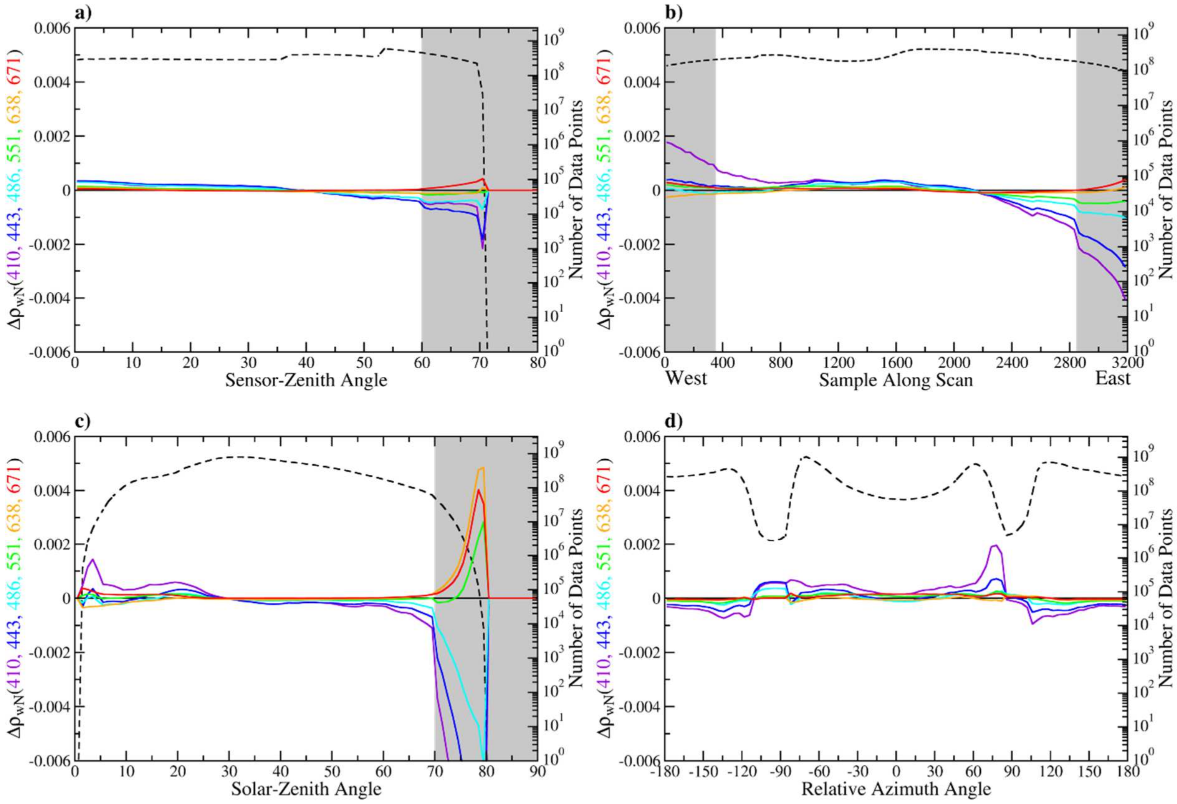

Figure 2. Dependence of $\Delta\rho_{wN}(\lambda)$ on (a) the sensor-zenith angle, (b) the sample along the scan, (c) the solar-zenith angle, and (d) the relative azimuth angle. The solid colored lines show the anomaly $\Delta\rho_{wN}(\lambda)$. The black dashed lines, along with the right ordinates, indicate the number of retrievals. The gray shaded areas in panels (a) and (b) indicate where the large sensor-zenith angle flag (> 60°) is triggered by MSL12 to warn about questionable data quality of retrievals. Similarly, the gray shaded areas in panel (c) indicate the large solar-zenith angle flag (> 70°) in MSL12.

Table 1. Mean absolute deviation of $\Delta\rho_{wN}(\lambda)$ for three ranges of sensor-zenith angle (θ).

	MAD[$\Delta\rho_{wN}(\lambda)$] × 10^4		
λ (nm)	$\theta \leq 20°$	$20° < \theta \leq 60°$	$\theta > 60°$
410	2.1	2.1	5.2
443	2.7	2.0	7.6
486	2.2	1.4	4.2
551	1.0	0.5	1.4
638	0.6	0.6	1.1
671	0.3	0.2	1.6

To quantify the deviations of $\Delta\rho_{wN}(\lambda)$ from zero, we show the results for the mean absolute deviation of $\Delta\rho_{wN}(\lambda)$ over the three ranges of sensor-zenith angle (less than 20°, 20° to 60°, and larger than 60°) in Table 1. Note that since $\Delta\rho_{wN}(\lambda)$ is an anomaly, its mean value over the entire range of the histogram is zero.

A closely related parameter to sensor-zenith angle is the position or sample along the scan. The VIIRS-SNPP swath extends up to about 3040 km across the direction of the flight path and is symmetric about the nadir. This corresponds to the sensor-zenith angle ranging from 0° at the center of the scan up to 70° at the swath edge. The VIIRS-SNPP medium spatial resolution bands (M-bands) used for ocean color retrievals have 3200 samples per scan. Figure 1b shows the dependence of $\Delta\rho_{wN}(\lambda)$ from the sample along the scan. Here, we count the number the samples in the direction from west to east, with the middle sample roughly corresponding to the nadir. Again, for most locations along the swath, the mean anomaly is minimal. However, near the swath edges, $\Delta\rho_{wN}(\lambda)$ is significantly increased. Predictably, the results are very similar to the sensor-zenith angle dependence. However, the sample along the scan dependence reveals more information, since it also captures asymmetry between the two sides of a scan, which would get averaged out on the sensor-zenith angle dependence (Fig. 2a). For this reason, we choose the sample along the scan in favor of sensor-zenith angle in the further discussion. Table 2 summarizes the results for the mean absolute deviation of $\Delta\rho_{wN}(\lambda)$ for the five regions along the swath, defined by the five ranges of sample numbers: [0–399], [399–1199], [1200–1999], [2000–2799], and [2800–3199].

Table 2. Mean absolute deviation of $\Delta\rho_{wN}(\lambda)$ for the five regions along the swath.

	MAD[$\Delta\rho_{wN}(\lambda)$] × 10^4				
λ (nm)	0–399	400–1199	1200–1999	2000–2799	2800–3199
410	13	3.7	2.1	4.7	26
443	2.5	1.8	2.6	3.7	19
486	0.7	1.0	2.1	2.3	8.3
551	1.3	1.2	0.9	1.6	4.5
638	1.7	0.6	0.6	0.9	0.6
671	1.7	0.6	0.4	0.7	1.1

Figure 2c shows the dependence with respect to the solar-zenith angle. Similar to the sensor-zenith angle dependence, we see significant deviations pointing to poor retrievals for values of the solar-zenith angle above 70°, which is also used as a threshold value in MSL12 for flagging the poor quality data due to this condition. In addition, we see some deviations from the average for very low values of solar-zenith angle. This corresponds to the relatively smaller number of retrievals in the tropics (only 1.3% of all retrievals have solar-zenith angle less than 10°), acquired almost exclusively on the west side of the scan (since VIIRS-SNPP is flying in the polar sun synchronous orbit with afternoon equatorial overpass). Thus, this deviation is also related to the sample across the scan dependence in Fig. 2b, for an approximate range of samples in the range 0–400. Table 3 summarizes the mean absolute deviations of $\Delta\rho_{wN}(\lambda)$ for the three ranges of solar-zenith angle: less than 20°, 20° to 70°, and larger than 70°.

Table 3. Mean absolute deviation of $\Delta\rho_{wN}(\lambda)$ for the three ranges of solar-zenith angle (θ_0).

	MAD[$\Delta\rho_{wN}(\lambda)$] × 10^4		
λ (nm)	$\theta_0 \le 20°$	$20° < \theta_0 \le 70°$	$\theta_0 > 70°$
410	4.7	2.0	5.2
443	1.4	1.7	3.2
486	1.0	0.8	1.6
551	1.0	0.5	0.2
638	0.9	0.4	0.6
671	1.3	0.1	0.4

The dependence of $\rho_{wN}(\lambda)$ anomaly on the relative azimuth angle is shown in Fig. 2d. We define it as an angle ranging from −180º to +180º between the azimuthal directions of the solar reflection and the sensor direction. Thus, a small (near zero) relative azimuth angle indicates a possibility of solar Fresnel reflection from water surface (sun glint) reaching the sensor (if solar- and sensor-zenith angles are similar). The number of data points shows two dips near ±90º. This is because near the equator, the relative azimuth angle can only fall within two narrow ranges of values corresponding to the samples on the east and the west side of the scan. For higher latitudes, these two ranges of the relative azimuth angle can broaden and also shift with a seasonal modulation. However, the two ranges of relative azimuth angle near ±90º do not have many retrievals. Unsurprisingly, with fewer data points for statistics, $\Delta\rho_{wN}(\lambda)$ also shows somewhat more noisy behavior near these two dips.

We also investigate how different combinations of geometric retrieval parameters affect the ocean color retrievals. In particular, we focus on the combined effect of different values of the solar-zenith angle and the sample along the scan. In Fig. 3a, we show the mean anomaly for the short-blue band $\rho_{wN}(410)$ with respect to both solar-zenith angle and the sample along the scan. Note that low values of solar-zenith angle are only possible for the westernmost part of the swath. The oval in dashed line indicates an approximate parameter region with high sun glint, and thus sharply decreased the number of retrievals and increased noise in the data. Significant deviations from average are encountered for the large values of solar-zenith angle, and near both edges of the swath. It appears that high solar-zenith angles have a more pronounced impact on retrievals in the eastern part of the swath. Figures 3b, 3c, and 3d show a very similar pattern for $\rho_{wN}(443)$, $\rho_{wN}(486)$, and the green band $\rho_{wN}(551)$, respectively, although the amplitude of the anomaly $\Delta\rho_{wN}(\lambda)$ is decreasing with increasing wavelength λ. Indeed, the similarity of patterns seen in Fig. 3 indicates that the $\rho_{wN}(\lambda)$ anomalies are quite correlated across the spectrum (*IOCCG*, 2010; *Wang and Gordon*, 2018).

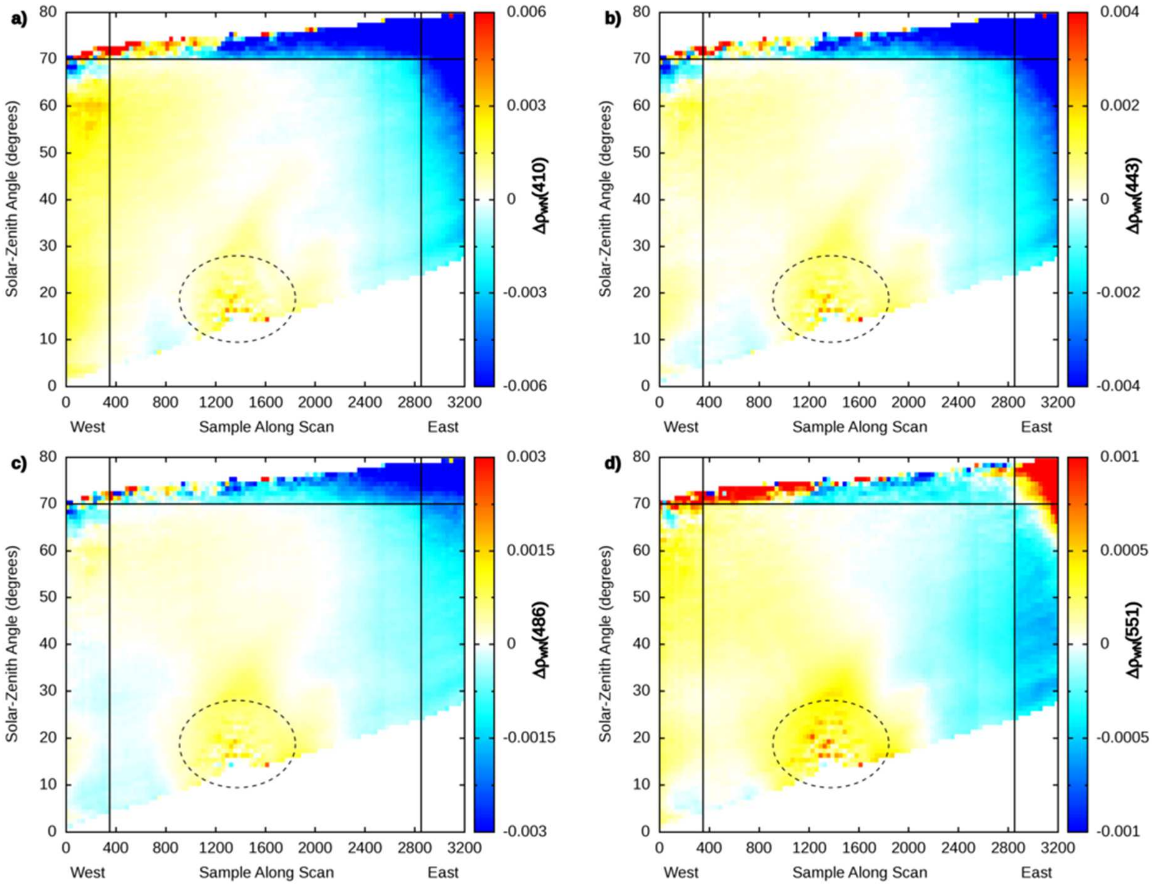

Figure 3. Dependence of $\Delta\rho_{wN}(\lambda)$ on the solar-zenith angle and the sample along the scan for (a) $\Delta\rho_{wN}(410)$, (b) $\Delta\rho_{wN}(443)$, (c) $\Delta\rho_{wN}(486)$, and (d) $\Delta\rho_{wN}(551)$. The dashed oval line indicates the parameter region with high sun glint conditions, where fewer retrievals result in more noisy data. The vertical lines indicate the boundary when sensor-zenith angle exceeds 60º, and the horizontal line indicates the onset of high solar-zenith angle at 70º.

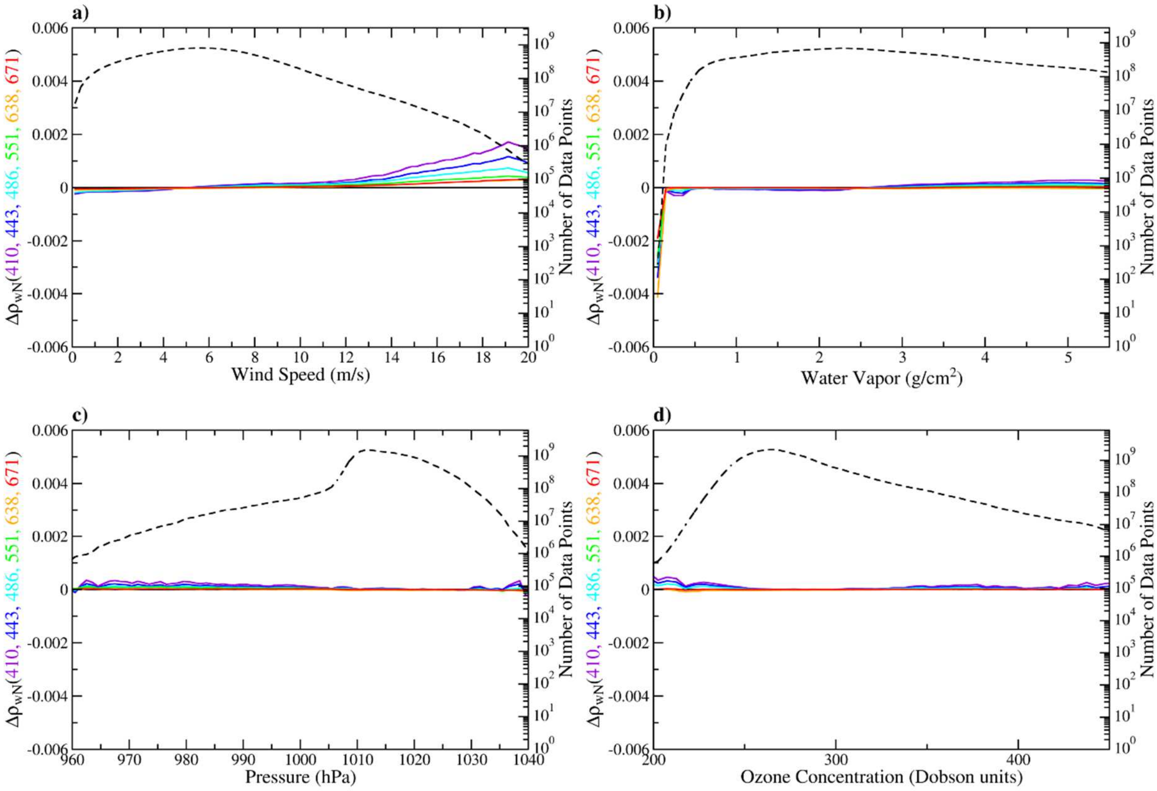

Figure 4. Dependence of $\Delta\rho_{wN}(\lambda)$ on (a) the wind speed, (b) the amount of water vapor in the atmosphere, (c) the sea level atmospheric pressure, and (d) the ozone concentration. The solid colored lines show $\Delta\rho_{wN}(\lambda)$. The black dashed lines, along with the right ordinates, indicate the number of retrievals.

3.2. Effects of ancillary data inputs

Next, we examine the statistical consistency with respect to some physical parameters affecting the ocean color retrievals. The results in the previous section confirm that good quality ocean color retrievals are obtained for solar-zenith angles and sensor-zenith angles of $\leq 70°$ and $\leq 60°$, respectively. Therefore, in the further analysis, we only use the ocean color retrievals with solar- and sensor-zenith angles meeting these requirements.

Figure 4a shows the dependence of the deviation or $\rho_{wN}(\lambda)$ anomaly $\Delta\rho_{wN}(\lambda)$ with respect to the surface wind speed. For wind speed up to about 14 m/s, the deviation from average value is negligible. However, it increases for higher wind speeds, which occur for a smaller number of retrievals. In the MSL12 ocean color data processing, there are three radiance components that require the input of wind speed for surface roughness characteristics, i.e., ocean whitecap radiance (*Gordon and Wang*, 1994b), sun glint radiance (*Wang and Bailey*, 2001), and Rayleigh scattering radiance (*Gordon and Wang*, 1992; *Wang*, 2002; 2016). However, examining the scenes with whitecaps in detail, we have concluded that MSL12 $\rho_{wN}(\lambda)$ spectra data are unchanged, or not impacted by the whitecaps radiance contribution with high wind speed. In fact, the TOA whitecap radiance contribution is generally not significant (*Moore et al.*, 2000). Other possible errors are from sun glint contamination correction (*Wang and Bailey*, 2001) that uses the Cox and Munk (*Cox and Munk*, 1954) model with the input of wind speed for sun glint radiance estimation, as well as Rayleigh scattering radiance computation that also uses the Cox and Munk model (*Cox and Munk*, 1954) for surface roughness (wind speed) (*Gordon and Wang*, 1992; *Wang*, 2002; 2016). Thus, it is possible that there may be some uncertainties related to the Cox and Munk (1954) model for high wind speed (*Zhang and Wang*, 2010). In addition, we note that high winds have a slight correlation with sparse clouds, which may increase variability in the satellite-retrieved $\rho_{wN}(\lambda)$ values.

Figure 4b shows the dependence on the amount of the water vapor in the atmospheric column. No obvious deviation is seen here, except for rarely encountered values of very low humidity, where insufficient data yields noisy results. Figure 4c similarly indicates no anomalous behavior with respect to the sea level atmospheric pressure, which is used as one of the inputs for the Rayleigh radiance computation (*Wang*, 2005; 2016). Likewise, Figure 4d shows no significant deviation with respect to the amount of the ozone in the atmosphere. Therefore, the MSL12 ocean color data processing system performed perfectly for VIIRS-derived $\rho_{wN}(\lambda)$ spectra with respect to the ancillary inputs of water vapor, ocean surface atmospheric pressure, and ozone amount, as well as to the wind speed up to about 14 m/s.

To better quantify the anomaly $\Delta\rho_{wN}(\lambda)$, we summarize the mean absolute deviation of $\Delta\rho_{wN}(\lambda)$ for wind speeds less than and exceeding 14 m/s in Table 4. We recall that the accuracy requirement for $\rho_{wN}(\lambda)$ at the blue 443 nm band is within ~0.001 (or 5%). From Table 4, MSL12 retrieved VIIRS-SNPP $\rho_{wN}(\lambda)$ spectra meet this goal even for high wind speeds.

Table 4. Mean absolute deviation of $\Delta\rho_{wN}(\lambda)$ for low and high wind speeds.

	MAD[$\Delta\rho_{wN}(\lambda)$] × 10^4	
λ (nm)	wind speed ≤ 14 m/s	wind speed > 14 m/s
410	1.1	8.6
443	0.8	5.9
486	0.6	4.2
551	0.3	2.5
638	0.3	1.5
671	0.2	1.6

3.3. Effects of intermediate retrieval parameters

The glint coefficient, computed from the Cox and Munk model (*Cox and Munk*, 1954; *Wang and Bailey*, 2001), is a more precise indicator of the degree to which the sun glint affects the retrievals. In addition to the combination of the solar- and sensor-zenith angles, and the relative azimuth angle, the glint coefficient computation also includes the wind speed, which affects the surface roughness, and thus also impacts sun reflection from the water surface (*Cox and Munk*, 1954; *Wang and Bailey*, 2001). The dependence on the glint coefficient in Fig. 5a shows some increase in $\Delta\rho_{wN}(\lambda)$ for stronger glint conditions.

Table 5. Mean absolute deviation of $\Delta\rho_{wN}(\lambda)$ for different ranges of AOD.

	MAD[$\Delta\rho_{wN}(\lambda)$] × 10^4			
λ (nm)	AOD < 0.1	0.1 < AOD ≤ 0.2	0.2 < AOD ≤ 0.3	AOD > 0.3
410	2.9	1.7	9.4	22
443	2.1	1.1	4.0	11
486	1.5	1.3	0.3	2.6
551	0.9	1.1	0.8	1.0
638	0.9	1.1	3.1	5.2
671	0.5	0.9	2.2	4.7

The AOD is a parameter quantifying the aerosols in the atmosphere above the retrieval location. Aerosol optical property data are by-products from atmospheric correction (*Gordon and Wang*, 1994a; *Wang, et al.*, 2005). The AOD measures the extent of light scattering and attenuation by aerosols. Higher AOD usually corresponds to more difficult retrieval conditions (*Gordon and Wang*, 1994a; *IOCCG*, 2010; *Wang*, 2007). In particular, cases with heavy aerosols such as smoke and dust are masked out. In these conditions, for AOD higher than 0.2, $\rho_{wN}(\lambda)$ spectra are slightly overestimated for the red bands, and they are slightly underestimated for the blue bands (Fig. 5b). However, for extremely low AOD cases (e.g., < 0.03) $\rho_{wN}(\lambda)$ spectra at the short wavelengths (410 and 443 nm) are also slightly underestimated (Fig. 5b). This is likely due to the correlations with other impact factors, e.g., cases with low aerosols in the Southern Ocean where retrievals are also associated with large solar-zenith angles (see Fig. 2c). Table 5 summarizes the mean absolute deviation of $\rho_{wN}(\lambda)$ for these four ranges of AOD: less than 0.1, 0.1–0.2, 0.2–0.3, and larger than 0.3. We note that for AOD ≤ 0.3, the mean anomalies of VIIRS-derived $\rho_{wN}(\lambda)$ spectra are mostly within ~0.0005, except for the short blue band $\rho_{wN}(410)$ with the value of ~0.001, which is significantly better than the accuracy requirement of ~0.001 (or 5%) for the blue band reflectance $\rho_{wN}(443)$.

The next panel, Fig. 5c, shows that reflectance anomaly $\Delta\rho_{wN}(\lambda)$ spectra are slightly elevated for retrievals within ~5–10 km from clouds. The remnants of the straylight effect (*Jiang and Wang*, 2013) are the most likely cause for this. Table 6 shows the increases in $\Delta\rho_{wN}(\lambda)$ for the three ranges (0–5 km, 5–15 km, and 15–30 km) of distance from the nearest cloud, using the average values for retrievals further than 30 km from clouds [$\Delta\rho_{wN}^{*}(\lambda)$] as baseline values. To confirm the effect of the proximity to the clouds, we have also repeated the same study by including the data affected by straylight and cloud shadow conditions. These results are shown in Fig. 5d, and indeed exhibit a more pronounced increase in $\Delta\rho_{wN}(\lambda)$ spectra for retrievals near clouds, as compared to Fig. 5c, where data affected by straylight and cloud shadow are masked out.

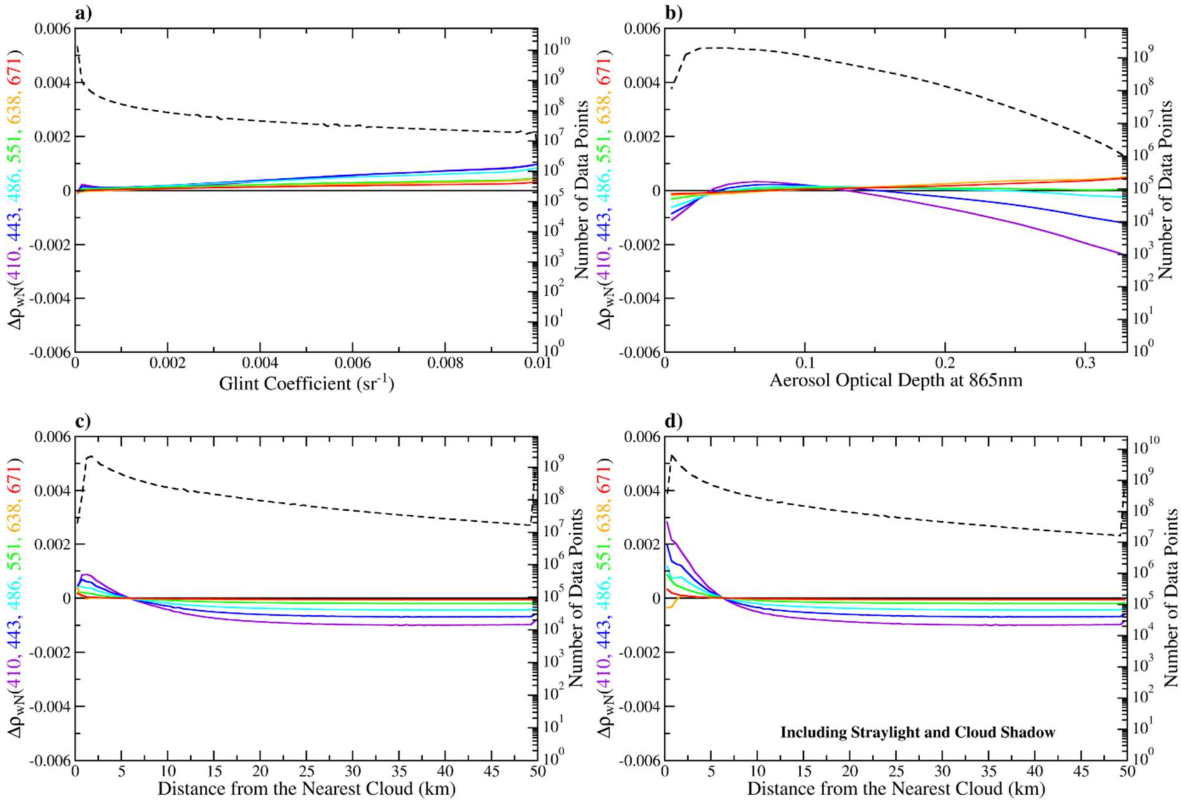

Figure 5. Dependence of $\Delta\rho_{wN}(\lambda)$ on (a) sun glint coefficient, (b) aerosol optical depth, (c) distance from the nearest cloud, and (d) distance from the nearest cloud, including the retrievals affected by straylight and cloud shadow conditions. The solid colored lines show $\Delta\rho_{wN}(\lambda)$. The black dashed lines, along with the right ordinates, indicate the number of retrievals.

Table 6. Mean absolute deviation of $\Delta\rho_{wN}(\lambda)$ for the three ranges of distance from the nearest cloud (DNC).

	MAD[$\Delta\rho_{wN}(\lambda) - \Delta\rho_{wN}^*(\lambda)$] × 10^4		
λ (nm)	DNC ≤ 5 km	5 km < DNC ≤ 15 km	15 km < DNC ≤ 30 km
410	15	6.3	0.5
443	11	4.4	0.4
486	6.8	2.8	0.3
551	3.1	1.3	0.2
638	0.3	0.3	0.0
671	0.4	0.4	0.1

3.4. Impact on derived biological and biogeochemical products

While normalized water-leaving reflectance $\rho_{wN}(\lambda)$ spectra are the central ocean color measurements, the impact of $\Delta\rho_{wN}(\lambda)$ on the $\rho_{wN}(\lambda)$-derived ocean biological and biogeochemical products, such as Chlorophyll-a concentration (*Hu, et al.*, 2012; *O'Reilly, et al.*, 1998; *Wang and Son*, 2016), and water diffuse attenuation coefficient at the wavelength of 490 nm $K_d(490)$ (*Wang, et al.*, 2009a), are also important to evaluate. Consequently, we want to estimate how much these derived quantities are affected by any systematic biases in $\rho_{wN}(\lambda)$ with respect to various retrieval parameters.

However, both Chl-a and $K_d(490)$ range over several orders of magnitude, and their frequency distributions are very skewed. Consequently, the mean anomaly is not a good measure for data consistencies, as it is heavily impacted by few infrequent localized events (such as algae blooms). In order to overcome this difficulty, we have instead opted to evaluate the median anomaly dependence on various retrieval parameters for Chl-a and $K_d(490)$.

Figure 6a shows the median anomaly for Chl-a and $K_d(490)$ versus the sample along the scan (also related to sensor-zenith angle), with little to no impact in the derived quantities for all values of this angle. This suggests that the calculation of Chl-a and $K_d(490)$ may be extended for larger values of sensor-zenith angle. However, in Fig. 6b, the dependence on solar-zenith angle shows significant positive bias for values larger than 70°, which is similar to the results for the reflectances in Fig. 2c. Thus, the systematic biases in reflectances for large solar-zenith angles translate into biases for the derived Chl-a and $K_d(490)$. The last two panels, Figs. 6c and 6d, show the dependence of the median anomaly in Chl-a and $K_d(490)$ with respect to the wind speed and the AOD. Comparing these with the results in Figs. 4a and 5b, respectively, we note that the derived quantities are overall less sensitive to the biases in the reflectance spectra. Results for other dependent variables (not shown) similarly show little to no systematic bias in derived Chl-a and $K_d(490)$. In fact, across the all the parameter ranges in Figs. 2, 4 and 5 (with the exception of solar-zenith angles exceeding 70°), the Chl-a anomaly is less than 0.01mg/m^3, and $K_d(490)$ anomaly is less than 0.005m^{-1}.

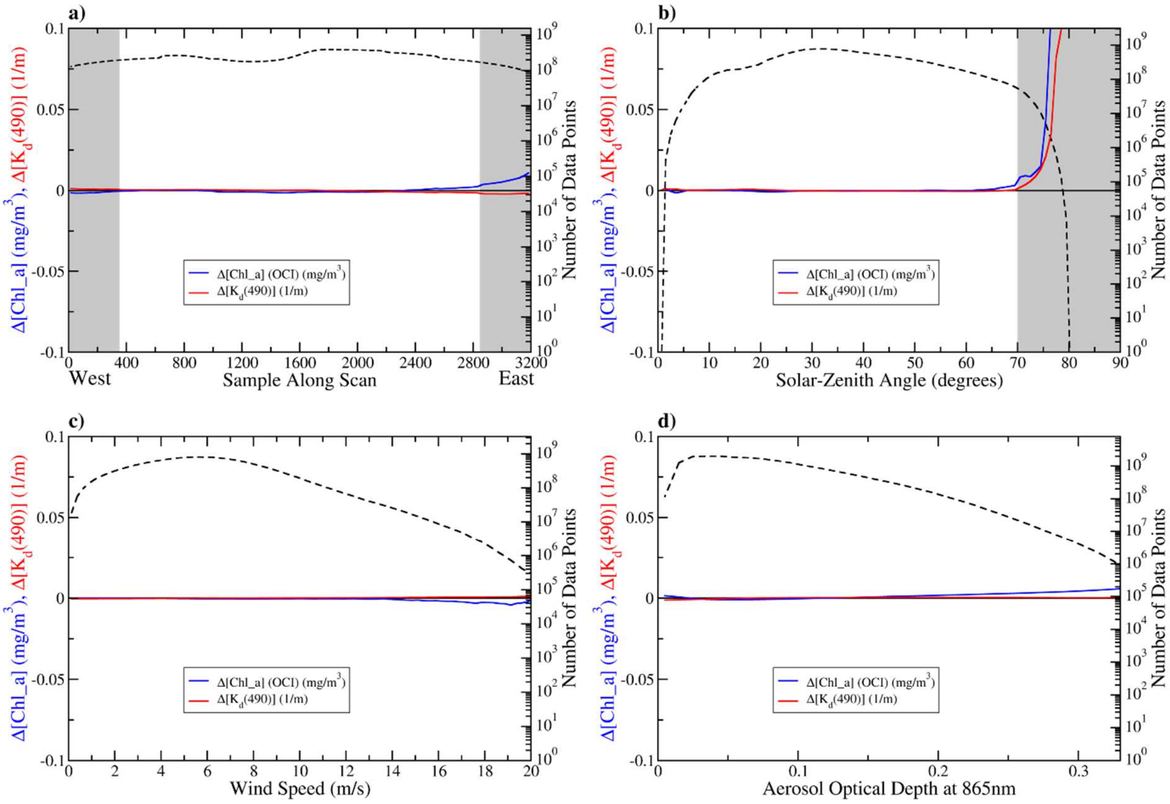

Figure 6. Dependence of Chl-a (OCI algorithm) and $K_d(490)$ on (a) the sample along the scan, (b) the solar-zenith angle, (c) the wind speed, and (d) the aerosol optical depth. The gray shaded areas in panel (a) indicate where the large sensor-zenith angle flag (> 60°) is set in MSL12. Similarly, the gray shaded areas in panel (b) indicate the large solar-zenith angle flag (> 70°) in MSL12.

4. Discussion

In the past, several studies for the regional ocean color data consistency have looked at the variability of ocean color spectra with respect to different retrieval parameters (e.g., *Barnes and Hu*, 2016). Instead, we have analyzed the deviation from the normal (average or median), or the anomaly, for the global deep waters which display high natural variability of the ocean color spectra across the different regions. To illustrate the importance of using the $\rho_{wN}(\lambda)$ spectra anomaly, or the deviation from average, to assess the global data statistical consistency, we have also repeated parts of this study using the $\rho_{wN}(\lambda)$ spectra directly, i.e., without subtracting the average values. Results (not shown) confirmed our expectations, i.e. satellite-derived $\rho_{wN}(\lambda)$ spectra are a function of environmental variables, as well as various solar-sensor geometry inputs. Thus, the variability of $\rho_{wN}(\lambda)$ is not a good measure of global data statistical consistency, and is only appropriate in regional studies where the natural variability of the ocean color spectra is rather small.

We have also analyzed the reflectance anomaly $\Delta\rho_{wN}(\lambda)$ with retrievals restricted to oligotrophic waters (areas where multi-year Chl-a average is less than 0.1 mg/m^3), which yield very similar results. Since the oligotrophic waters do not extend to latitudes 40° from the equator, the values of the solar-zenith angle are also generally smaller, and the retrieval conditions are overall better. This is reflected in lower anomaly across the swath dependence. The dependences on the physical ancillary parameters are also very close to those from the global deep water discussed in the previous sections. Furthermore, we have also repeated the analysis by restricting the retrievals to those with QA score (*Wei et al.*, 2016) higher than 0.6. These results are even closer to those described in the previous sections, with only slightly smaller systematic biases for the retrievals with high solar zenith angle and high wind speed.

It is noted that while the method in this study identifies anomalies in ocean color data retrievals, it does not identify the exact sources of data inconsistencies. For example, this analysis cannot distinguish between inconsistencies introduced by suboptimal sensor calibration, and various parts of the atmospheric correction and retrieval algorithms. Any correlation of the deviations in anomaly with particular retrieval parameters should be seen only as a hint for what part of the retrieval process might need a further examination. Furthermore, although we have attempted to investigate the dependencies with respect to the most relevant retrieval parameters, these results are not exhaustive in the sense that there may be other significant parameters or combinations of parameters that provide yet more information on the quality and consistency of the retrievals.

5. Conclusions

We have analyzed recently reprocessed VIIRS-SNPP ocean color data for the entire 2016 year for statistical consistency over the global deep ocean. The results show very small to negligible deviations from average values for most retrieval parameters. We note somewhat increased $\rho_{wN}(\lambda)$ spectra in all bands for higher wind speed (> 14 m/s), and also in areas close to clouds, likely due to the effect of straylight. We also find that $\rho_{wN}(\lambda)$ for the blue bands are underestimated in the areas with heavy aerosol presence in atmosphere, while the red band is overestimated in those conditions.

We have also demonstrated how the analysis presented in this work can be used to identify and distinguish the regions of parameters (such as solar- and sensor-zenith angles) with a systematic bias in the retrieved data, and how different versions of retrieval algorithms can be evaluated based on retrieval consistency. Although this study only covers one year of data, we have not observed any significant changes in any of our results for different years in previous studies. Also, further analysis shows that varying the time and length scale of the average values used to calculate the anomaly does not significantly impact the results presented in this study. While the list of retrieval parameters considered and investigated in this study is not exhaustive, it provides a comprehensive test for data statistical consistency, and means to identify the systematic biases. This is particularly helpful in the design of better and more precise satellite ocean color retrieval algorithms, as well as identification of what areas to look into where these algorithms can be improved.

Acknowledgments

This work was supported by the Joint Polar Satellite System (JPSS) funding. We thank two anonymous reviewers for their useful comments. The views, opinions, and findings contained in this paper are those of the authors and should not be construed as an official NOAA or U.S. Government position, policy, or decision.

References

Angstrom, A. (1929), On the atmospheric transmission of sun radiation and on dust in the air, *Geografiska Annaler*, *11*, 156–166.

Bailey, S. W., Franz, B. A., and Werdell, P. J. (2010), Estimation of near-infrared water-leaving reflectance for satellite ocean color data processing, *Opt. Express*, *18*, 7521–7527.

Barnes, B. B., Cannizzaro, J. P., English, D. C., and Hu, C. (2019), Validation of VIIRS and MODIS reflectance data in coastal and oceanic waters: An assessment of methods, *Remote Sens. Environ.*, *220*, 110–123.

Barnes, B. B., and Hu, C. (2016), Dependence of satellite ocean color data products on viewing angles: A comparison between SeaWiFS, MODIS, and VIIRS, *Remote Sens. Environ.*, *175*, 120–129.

Campbell, J. W., Blaisdell, J. M., and Darzi, M. (1995), Level-3 SeaWiFS Data Products: Spatial and Temporal Binning Algorithms,Vol. 32, NASA Tech. Memo. 104566, S.B. Hooker, E.R. Firestone, and J.G. Acker, Eds., p, NASA Goddard Space Flight Center, Greenbelt, Maryland.

Cao, C., Xiong, X., Blonski, S., Liu, Q., Uprety, S., Shao, X., Bai, Y., and Weng, F. (2013), Suomi NPP VIIRS sensor data record verification, validation, and long-term performance monitoring, *J. Geophys. Res. Atmos.*, *118*, 11664–11678.

Clark, D. K., Gordon, H. R., Voss, K. J., Ge, Y., Broenkow, W., and Trees, C. (1997), Validation of atmospheric correction over the ocean, *J. Geophys. Res.*, *102*, 17209–17217.

Cox, C., and Munk, W. (1954), Measurements of the roughness of the sea surface from photographs of the sun's glitter, *Jour. Opt. Soc. of Am.*, *44*, 838–850.

Goldberg, M. D., Kilcoyne, H., Cikanek, H., and Mehta, A. (2013), Joint Polar Satellite System: The United States next generation civilian polar-orbiting environmental satellite system, *J. Geophys. Res. Atmos.*, *118*, 13463–13475.

Gordon, H. R. (2005), Normalized water-leaving radiance: revisiting the influence of surface roughness, *Appl. Opt.*, *44*, 241–248.

Gordon, H. R., and Wang, M. (1992), Surface roughness considerations for atmospheric correction of ocean color sensors. 1: The Rayleigh scattering component, *Appl. Opt.*, *31*, 4247–4260.

Gordon, H. R., and Wang, M. (1994a), Retrieval of water-leaving radiance and aerosol optical thickness over the oceans with SeaWiFS: A preliminary algorithm, *Appl. Opt.*, *33*, 443–452.

Gordon, H. R., and Wang, M. (1994b), Influence of oceanic whitecaps on atmospheric correction of ocean-color sensor, *Appl. Opt.*, *33*, 7754–7763.

Hlaing, S., Harmel, T., Gilerson, A., Foster, R., Weidemann, A., Arnone, R., Wang, M., and Ahmed, S. (2013), Evaluation of the VIIRS ocean color monitoring performance in coastal regions, *Remote Sens. Environ.*, *139*, 398–414.

Hu, C., Lee, Z., and Franz, B. A. (2012), Chlorophyll a algorithms for oligotrophic oceans: A novel approach based on three-band reflectance difference, *J. Geophys. Res.*, *117*, C01011, doi: 01010.01029/02011JC007395.

IOCCG (Ed.) (2010), *Atmospheric Correction for Remotely-Sensed Ocean-Colour Products*, IOCCG, Dartmouth, Canada.

Jiang, L., and Wang, M. (2013), Identification of pixels with stray light and cloud shadow contaminations in the satellite ocean color data processing, *Appl. Opt.*, *52*, 6757–6770.

Jiang, L., and Wang, M. (2014), Improved near-infrared ocean reflectance correction algorithm for satellite ocean color data processing, *Opt. Express*, *22*, 21657–21678.

King, M. D., Platnick, S., Menzel, W. P., Ackerman, S. A., and Hubanks, P. A. (2013), Spatial and temporal distribution of clouds observed by MODIS onboard the Terra and Aqua satellites, *IEEE Trans. Geosci. Remote Sens.*, *51*, 3826–3852.

Lee, Z. P., Du, K., and Arnone, R. (2005), A model for the diffuse attenuation coefficient of downwelling irradiance, *J. Geophys. Res.*, *110*, C02016, doi:10.1029/2004JC002275.

McClain, C. R. (2009), A decade of satellite ocean color observations, *Annu. Rev. Mar. Sci.*, *1*, 19–42.

Mikelsons, K., and Wang, M. (2019), Optimal satellite orbit configuration for global ocean color product coverage, *Opt. Express*, *27*, A445–A457.

Mikelsons, K., Wang, M., Jiang, L., and Bouali, M. (2014), Destriping algorithm for improved satellite-derived ocean color product imagery, *Opt. Express*, *22*, 28058–28070.

Moore, K. D., Voss, K. J., and Gordon, H. R. (2000), Spectral reflectance of whitecaps: Their contribution to water-leaving radiance, *J. Geophys. Res.*, *105*, 6493–6499.

Morel, A., and Gentili, G. (1996), Diffuse reflectance of oceanic waters. III. Implication of bidirectionality for the remote-sensing problem, *Appl. Opt.*, *35*, 4850–4862.

O'Reilly, J. E., Maritorena, S., Mitchell, B. G., Siegel, D. A., Carder, K. L., Garver, S. A., Kahru, M., and McClain, C. R. (1998), Ocean color chlorophyll algorithms for SeaWiFS, *J. Geophys. Res.*, *103*, 24937–24953.

Ramachandran, S., and Wang, M. (2011), Near-real-time ocean color data processing using ancillary data from the Global Forecast System model, *IEEE Trans. Geosci. Remote Sens.*, *49*, 1485–1495.

Ruddick, K. G., Ovidio, F., and Rijkeboer, M. (2000), Atmospheric correction of SeaWiFS imagery for turbid coastal and inland waters, *Appl. Opt.*, *39*, 897–912.

Son, S., and Wang, M. (2015), Diffuse attenuation coefficient of the photosynthetically available radiation Kd(PAR) for global open ocean and coastal waters, *Remote Sens. Environ.*, *159*, 250–258.

Sun, J., and Wang, M. (2015), Radiometric calibration of the VIIRS reflective solar bands with robust characterizations and hybrid calibration coefficients, *Appl. Opt.*, *54*, 9331–9342.

Sun, J., and Wang, M. (2016), VIIRS reflective solar bands calibration progress and its impact on ocean color products, *Remote Sens.*, *8*, 194, doi: 10.3390/rs8030194.

Thuillier, G., Herse, M., Labs, D., Foujols, T., Peetermans, W., Gillotay, D., Simon, P. C., and Mandel, H. (2003), The solar spectral irradiance from 200 to 2400 nm as measured by the SOLSPEC spectrometer from the ATLAS and EURECA missions, *Sol. Phys.*, *214*, 1–22.

Wang, M. (2002), The Rayleigh lookup tables for the SeaWiFS data processing: Accounting for the effects of ocean surface roughness, *Int. J. Remote Sens.*, *23*, 2693–2702.

Wang, M. (2005), A refinement for the Rayleigh radiance computation with variation of the atmospheric pressure, *Int. J. Remote Sens.*, *26*, 5651–5663.

Wang, M. (2006), Effects of ocean surface reflectance variation with solar elevation on normalized water-leaving radiance, *Appl. Opt.*, *45*, 4122–4128.

Wang, M. (2007), Remote sensing of the ocean contributions from ultraviolet to near-infrared using the shortwave infrared bands: simulations, *Appl. Opt.*, *46*, 1535–1547.

Wang, M. (2016), Rayleigh radiance computations for satellite remote sensing: Accounting for the effect of sensor spectral response function, *Opt. Express*, *24*, 12414–12429.

Wang, M., and Bailey, S. (2001), Correction of the sun glint contamination on the SeaWiFS ocean and atmosphere products, *Appl. Opt.*, *40*, 4790–4798.

Wang, M., and Gordon, H. R. (2018), Sensor performance requirements for atmospheric correction of satellite ocean color remote sensing, *Opt. Express*, *26*, 7390–7403.

Wang, M., Isaacman, A., Franz, B. A., and McClain, C. R. (2002), Ocean color optical property data derived from the Japanese Ocean Color and Temperature Scanner and the French Polarization and Directionality of the Earth's Reflectances: A comparison study, *Appl. Opt.*, *41*, 974–990.

Wang, M., and Jiang, L. (2018), Atmospheric correction using the information from the short blue band, *IEEE Trans. Geosci. Remote Sens.*, *56*, 6224–6237.

Wang, M., Knobelspiesse, K. D., and McClain, C. R. (2005), Study of the Sea-Viewing Wide Field-of-View Sensor (SeaWiFS) aerosol optical property data over ocean in combination with the ocean color products, *J. Geophys. Res.*, *110*, D10S06, doi:10.1029/2004JD004950.

Wang, M., Liu, X., Tan, L., Jiang, L., Son, S., Shi, W., Rausch, K., and Voss, K. (2013), Impact of VIIRS SDR performance on ocean color products, *J. Geophys. Res. Atmos.*, *118*, 10347–10360, doi:10.1002/jgrd.50793.

Wang, M., and Shi, W. (2006), Cloud masking for ocean color data processing in the coastal regions, *IEEE Trans. Geosci. Remote Sens.*, *44*, 3196–3205.

Wang, M., Shi, W., and Jiang, L. (2012), Atmospheric correction using near-infrared bands for satellite ocean color data processing in the turbid western Pacific region, *Opt. Express*, *20*, 741–753.

Wang, M., Shi, W., Jiang, L., and Voss, K. (2016), NIR- and SWIR-based on-orbit vicarious calibrations for satellite ocean color sensors, *Opt. Express*, *24*, 20437–20453.

Wang, M., and Son, S. (2016), VIIRS-derived chlorophyll-a using the ocean color index method, *Remote Sens. Environ.*, *182*, 141–149.

Wang, M., Son, S., and L. W. Harding, J. (2009a), Retrieval of diffuse attenuation coefficient in the Chesapeake Bay and turbid ocean regions for satellite ocean color applications, *J. Geophys. Res.*, *114*, C10011, http://dx.doi.org/10.1029/2009JC005286.

Wang, M., Son, S., and Shi, W. (2009b), Evaluation of MODIS SWIR and NIR-SWIR atmospheric correction algorithm using SeaBASS data, *Remote Sens. Environ.*, *113*, 635–644.

Wei, J., Lee, Z., and Shang, S. (2016), A system to measure the data quality of spectral remote-sensing reflectance of aquatic environments, *J. Geophys. Res. Oceans*, *121*, 8189–8207, doi:10.1002/2016JC012126.

Werdell, P. J., and Bailey, S. W. (2005), An improved in-situ bio-optical data set for ocean color algorithm development and satellite data product validation, *Remote Sens. Environ.*, *98*, 122–140.

Zhang, H., and Wang, M. (2010), Evaluation of sun glint models using MODIS measurements, *J. Quant. Spectrosc. Radiat. Transf.*, *111*, 492–506.

Zibordi, G., Holben, B. N., Slutsker, I., Giles, D., D'Alimonte, D., Melin, F., Berthon, J.-F., Vandemark, D., Feng, H., Schuster, G., Fabbri, B. E., Kaitala, S., and Seppala, J. (2009), AERONET-OC: a network for the validation of ocean color primary radiometric products, *J. Atmos. Ocean Technol.*, *26*, 1634–1651.

Zibordi, G., Melin, F., and Berthon, J.-F. (2006), Comparison of SeaWiFS, MODIS and MERIS radiometric products at a coastal site, *Geophy. Res. Lett.*, *33*, L06617, doi:10.1029/2006GL025778.

Zibordi, G., Melin, F., Voss, K., Johnson, B. C., Franz, B. A., Kwiatkowska, E., Huot, J. P., Wang, M., and Antoine, D. (2015), System vicarious calibration for ocean color climate change applications: Requirements for in situ data, *Remote Sens. Environ.*, *159*, 361–369.